SCIENCE CHINA
Earth Sciences

• RESEARCH PAPER •

doi: 10.1007/s11430-015-5056-z

Modeling the Earth's magnetosphere under the influence of solar wind with due northward IMF by the AMR-CESE-MHD model

WANG Juan[1], DU AiMin[2*], ZHANG Ying[2], ZHANG TieLong[3] & GE YaSong[2]

[1] *State Key Laboratory of Space Weather, Center for Space Science and Applied Research, Chinese Academy of Sciences, Beijing 100190, China;*
[2] *Key Laboratory of Earth and Planetary Physics, Institute of Geology and Geophysics, Chinese Academy of Sciences, Beijing 100029, China;*
[3] *Space Research Institute, Austrian Academy of Sciences, Graz 8042, Austria*

Received September 12, 2014; accepted November 21, 2014

We present a newly developed global magnetohydrodynamic (MHD) model to study the responses of the Earth's magnetosphere to the solar wind. The model is established by using the space-time conservation element and solution element (CESE) method in general curvilinear coordinates on a six-component grid system. As a preliminary study, this paper is to present the model's numerical results of the quasi-steady state and the dynamics of the Earth's magnetosphere under steady solar wind flow with due northward interplanetary magnetic field (IMF). The model results are found to be in good agreement with those published by other numerical magnetospheric models.

numerical simulation, magnetosphere, magnetohydrodynamic model, adaptive mesh refinement technique, the space-time conservation element and solution element method

Citation: Wang J, Du A M, Zhang Y, et al. 2015. Modeling the Earth's magnetosphere under the influence of solar wind with due northward IMF by the AMR-CESE-MHD model. Science China: Earth Sciences, doi: 10.1007/s11430-015-5056-z

It is significant to understand the energy transfer process in geospace or the interaction of the solar wind-magnetosphere-ionosphere (S-M-I) system, because the development of space weather starts basically from such studies. As a powerful modeling tool for understanding space weather, MHD simulations make up the limitations of single-point measurements provided by a spacecraft. Numberless investigations have been carried out for the simulations of the dynamics and configurations of the Earth's magnetosphere under due northward and southward IMF since the seminal paper of Dungey (1961). After decades' development, several global magnetospheric MHD models have been showed in literature. All these models have been established by solving certain forms of the MHD equations with somewhat different numerical techniques, such as the GEDAS model (Ogino et al., 1994), the Tanaka model (Tanaka, 1994), the Block-Adaptive Tree Solar-wind Roe-type Upwind Scheme (BATS-R-US) (Powell et al., 1999), the Grand Unified Magnetosphere-Ionosphere Coupling Simulation, version 4 (GUMICS-4) (Janhunen et al., 2012), the Lyon-Fedder-Mobarry (LFM) model (Lyon et al., 2004), the Space Weather Modelling Framework (SWMF) (Tóth et al., 2005; Rae et al., 2010; Liu et al., 2012; Lu et al., 2011, 2013; Jing et al., 2014), the Open General Geospace Circulation Model (OpenGGCM) (Raeder, 2003) and Piecewise Parabolic Method with a Lagrangian Remap MHD (PPMLR-MHD) model (Hu et al., 2005; Wang et al., 2012).

In the early stage, the MHD simulations of the solar wind interaction with magnetosphere and ionosphere were carried out theoretically by using constant solar wind and IMF as input. But in recent years, researchers have tried to model real magnetospheric events by using global MHD simulations with comparison against in situ measurements. In

*Corresponding author (email: amdu@mail.iggcas.ac.cn)

these studies, realistic solar wind parameters from observations were taken as the input to the MHD models.

Although long periods of steady solar wind with due northward or southward IMF rarely appear, the quasi-steady state of the magnetospheric configurations under such conditions still draw much attention because they are typical states of the highly dynamic magnetosphere. Thus, this scenario is what we follow to validate our new model. The AMR-CESE-MHD model has been developed for studying the solar-interplanetary and the solar active region (e.g., Feng et al. (2007); Feng et al. (2012a, 2014) and references therein). In this paper, we accommodate it to study the basic physical dynamic processes of the interaction of the solar wind-magnetosphere-ionosphere system.

1 Model equations and numerical implementation

In this section, the model equations used for studying the interaction between the solar wind and the Earth's magnetosphere and the AMR-CESE-MHD method for numerically solving the model are described briefly.

1.1 Model equations

The AMR-CESE-MHD model for the Earth's magnetosphere is a global coupled model of Earth's magnetosphere and ionosphere. The magnetosphere part solves the MHD equations as an initial-boundary-value problem in the region from 3 to 156 R_E, while the region within 3 R_E is treated as a magnetosphere-ionosphere coupling region. The physical processes in this region are parameterized using simple models and relationships. Using constant and uniform Pedersen conductance and neglecting the Hall conductance, we obtain the ionospheric potential through current conservation.

The governing equations can be described below:

$$\frac{\partial \mathbf{U}}{\partial t}+\left[\nabla\cdot\left(\tilde{\mathbf{F}}-\tilde{\mathbf{F}}_{\mathrm{v}}\right)\right]^{\mathrm{T}}=\mathbf{S}, \tag{1}$$

where the state vector, flux tensor, diffusive control terms and Powell source terms are

$$\mathbf{U}=\begin{bmatrix}\rho\\ \rho\,\mathbf{u}\\ \mathbf{B}_1\\ e_1\end{bmatrix}, \tag{2}$$

$$\tilde{\mathbf{F}}=\begin{bmatrix}\rho\,\mathbf{u}\\ \rho\,\mathbf{uu}+\mathbf{I}\left(p+\frac{1}{2}\mathbf{B}_1^2+\mathbf{B}_1\cdot\mathbf{B}_d\right)-\mathbf{B}_1\mathbf{B}_1-\mathbf{B}_1\mathbf{B}_\mathbf{d}-\mathbf{B}_\mathbf{d}\mathbf{B}_1\\ \mathbf{uB}-\mathbf{Bu}\\ \mathbf{u}\left(e_1+p+\frac{1}{2}\mathbf{B}_1^2+\mathbf{B}_1\cdot\mathbf{B}_d\right)-(\mathbf{u}\cdot\mathbf{B}_1)\mathbf{B}\end{bmatrix}^{\mathrm{T}}, \tag{3}$$

$$\tilde{\mathbf{F}}_{\mathrm{v}}=\begin{bmatrix}0\\ 0\\ \mathbf{I}\left(\upsilon\ \nabla\cdot\mathbf{B}_1\right)\\ 0\end{bmatrix}^{\mathrm{T}},\qquad \mathbf{S}=-\nabla\cdot\mathbf{B}_1\begin{bmatrix}0\\ \mathbf{B}\\ \mathbf{u}\\ \mathbf{u}\cdot\mathbf{B}_1\end{bmatrix}, \tag{4}$$

where ρ, $\mathbf{u}$, p, $\mathbf{B}(\equiv\mathbf{B}_1+\mathbf{B}_\mathrm{d})$ are the mass density, velocity, thermal pressure, magnetic field, $\mathbf{I}$ is a unit tensor, the ratio of specific heats γ is taken to be 5/3, and the energy density is $e_1=\frac{\rho\,\mathbf{u}^2}{2}+\frac{p}{\gamma-1}+\frac{\mathbf{B}_1^2}{2}$.

Our model is especially designed to simulate planets with strong intrinsic magnetic field which solves the deviation of the magnetic field from the intrinsic dipole field, that is, $\mathbf{B}$ is split into time-dependent derived part $\mathbf{B}_1$ and time-independent part $\mathbf{B}_\mathrm{d}$ (Tanaka, 1994), where $\mathbf{B}_\mathrm{d}$ corresponds to the Earth's intrinsic dipole field with a magnitude of 3.12×10^{-5} T at the equatorial surface.

The Powell source terms $-\nabla\cdot\mathbf{B}_1\left(0,\ \mathbf{B},\ \mathbf{u},\ \mathbf{u}\cdot\mathbf{B}_1\right)$ (Powell et al., 1999) and the diffusive control terms $\nabla\left(\nu\nabla\cdot\mathbf{B}_\mathbf{1}\right)$ (Feng et al., 2011) have been added to the MHD eq. (1) to deal with the divergence of the magnetic field. Here, following Feng et al. (2001), $\nu=1.3\left(\frac{1}{\Delta x^2}+\frac{1}{\Delta y^2}+\frac{1}{\Delta z^2}\right)^{-1}$, where Δx, Δy, Δz are grid spacings in Cartesian coordinates.

At the outer boundary, fixed inflow boundary conditions are applied at the dayside, while free flow boundary conditions are used at the nightside. At the inner boundary, the density and pressure are set to fixed values, the radial component of velocity is set to zero, and the tangential component of velocity is determined by the coupling between the magnetospheric inner boundary and the ionosphere to be discussed below. The normal component of time-dependent derived part of magnetic field $\mathbf{B_1}$ is determined by Dirichlet condition and its tangential components are determined by Neumann condition (Song et al., 1999).

The sunward side of the inflow plane at $x=-15.0\ R_E$ is initialized by solar wind parameters. For the earthward side, the magnetic field is initialized by the superposition of dipole magnetic field and mirror dipole magnetic field to create $B_x=0$ surface at the inflow plane referring to Raeder (2003) and the initial conditions for the density and plasma pressure are in accordance with Ogino (1986).

The parameters of the steady solar wind used for the model input are described as

$$\begin{aligned}&\rho=5\ \mathrm{cm}^{-3},\quad u_{\mathrm{xsw}}=-400\ \mathrm{km\,s}^{-1},\\ &T_{\mathrm{sw}}=2.321\times10^5\ \mathrm{K},\quad B_{\mathrm{zsw}}=5\ \mathrm{nT},\end{aligned} \tag{5}$$

where x is directed from the Earth to the Sun and z is directed from the center of the Earth to its Northern Hemi-

sphere.

The coupling between the magnetosphere and the ionosphere was established by mapping field-aligned currents from the magnetosphere to the ionosphere (Raeder et al., 1998). The ionosphere is treated as a two-dimensional spherical shell at 1.017 R_E. Thus a potential equation for the ionosphere is then solved according to Raeder (2003):

$$\nabla \cdot \boldsymbol{\Sigma} \cdot \nabla \Phi = -j_{//i} \left| \sin I \right|, \tag{6}$$

where Φ is the ionospheric potential, and I denotes the dipole magnetic field inclination angle at the ionosphere. And Σ denotes the tensor of the ionospheric conductances written as

$$\boldsymbol{\Sigma} = \begin{pmatrix} \Sigma_{\theta\theta} & \Sigma_{\theta\varphi} \\ -\Sigma_{\theta\varphi} & \Sigma_{\varphi\varphi} \end{pmatrix}, \tag{7}$$

where

$$\Sigma_{\theta\theta} = \frac{\Sigma_P}{\sin^2 I}, \quad \Sigma_{\theta\varphi} = \frac{\Sigma_H}{\sin I}, \quad \Sigma_{\varphi\varphi} = \Sigma_P, \tag{8}$$

where $\boldsymbol{\Sigma}_P$ and $\boldsymbol{\Sigma}_H$ are the Pedersen conductance and the Hall conductance respectively. In the present study, we set the Pedersen conductance to be 5 S and uniform at the northern and southern ionospheres, and for simplicity, we neglect the Hall conductance.

We assume the magnetic field is dipole and equipotential in the region between the inner boundary and the ionosphere. In order to obtain the field-aligned currents at the ionosphere, the perpendicular currents are neglected (Merkin and Lyon, 2010). From current continuity it follows that $j_{//}/B = \text{const}$ along the magnetic field lines between the magnetospheric inner boundary and the ionosphere. Consequently, the field-aligned currents at the ionosphere for eq. (6) can be written as $j_{//i} = \sigma j_{//m}$, where $j_{//i}$ and $j_{//m}$ are the field-aligned currents at the ionosphere and the magnetospheric inner boundary, σ is the ratio of the magnetic field strength at the ionosphere and the magnetospheric inner boundary. Thus, the field-aligned currents are mapped from the magnetospheric inner boundary to the ionosphere.

In the present model, we take the assumption that the ionospheric potential is a constant at or near the low-latitude boundary of the computational domain. The computational domain of eq. (6) is $(0 \leqslant \theta < 31.2^\circ) \cap (0 \leqslant \varphi \leqslant 180^\circ)$. With the conductances and the mapped the field-aligned currents at the ionosphere, we solve eq. (6) by using the chasing method. Then, according to Gombosi et al. (1998), the potential at the ionosphere is mapped along the magnetic field lines to the magnetospheric inner boundary. And the potential at the inner boundary is used to get the flow velocity by taking $\mathbf{u}_t = -(\nabla \Phi \times \mathbf{B}/\mathbf{B}^2)_t$ as the boundary conditions, here the subscript "t" refers to the tangential components of the velocity at the inner boundary. Thus the ionosphere plays a significant role in controlling the magnetospheric convection.

1.2 Numerical implementation

The AMR-CESE-MHD code (Feng et al., 2010, 2011) is employed in the present paper to numerically solve the model eq. (1). In this method, the governing MHD eq. (1) is transformed from the physical space (x, y, z) to the reference space (ξ, η, ζ) while retaining the conservation form. The CESE solver is used to solve the transformed equations in the reference space with simple rectangular-uniform mesh, where a parallel AMR package, PARAMESH (MacNeice et al., 2000), can be easily implemented. Because of the versatility of the general curvilinear coordinates, the method can be applied on any form of computational grid so long as it is locally Cartesian and its nonsingular transformation (mapping from physical space to reference space) is given. For details, refer to Feng et al. (2007, 2010, 2012b, 2013, 2014) and the references therein. In what follows for self-consistent description, we briefly report its realization on the six-component overlapping grids.

In the six-component grid introduced by Feng et al. (2010) for the solar-wind study, the spherical-shell computational domain is decomposed into six identical components with partial overlapping regions (Figure 1 of Feng et al. (2010)), and each component is identically defined by a low-latitude spherical domain

$$\left(\frac{\pi}{4} - \delta \leqslant \theta \leqslant \frac{3\pi}{4} + \delta\right) \cap \left(\frac{3\pi}{4} - \delta \leqslant \varphi \leqslant \frac{5\pi}{4} + \delta\right).$$

The parameter $\delta = 2\Delta\theta$ is determined by the grid spacing and layers of guard cells required for the minimum overlapping area of two grid sizes. In the six-component grid partitions, the same metric can be used and the component grids can be transformed into each other by coordinate transformation such that the basic equations, numerical grid distribution, and all numerical tasks are identical in each component. Hence we do not have to distinguish them and we only need to describe the grid partition and the associated coordinate transform. The grid points in both θ and φ directions are even spaced such that $\Delta\theta = \Delta\varphi$. In the r direction, a new variable ξ is introduced as a reference coordinate, which is exponentially related with r by $r = a^{\xi}$. In this way, the grid spacing $[\Delta r]$ in the r direction is always around $r\Delta\theta$ by choosing $\Delta\xi = \log_a(1+\Delta\theta)$, so that each grid cell is always approximately a cube. As pointed out by Feng et al. (2012a), the reference coordinates (ξ, η, ζ) used in our CESE solver refer to (ξ, η, φ) here, and with this setting, the grid cell in the reference space (ξ, η, ζ) is a rectangular box. In principle, any parameter $a > 1$ can be chosen and we take $a = 1.481$ as done by Feng et al. (2012a).

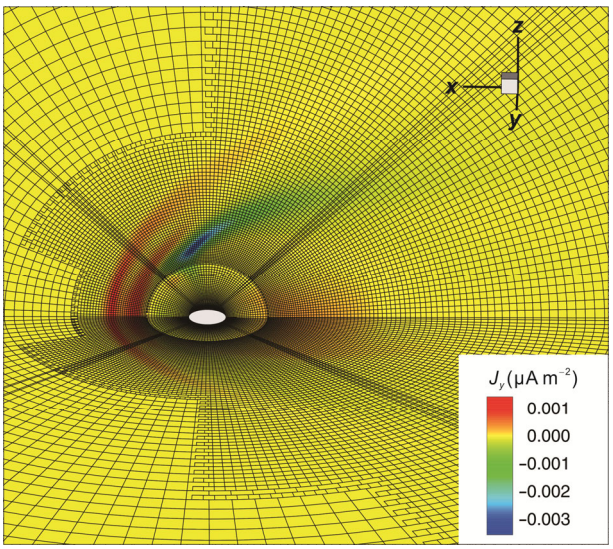

Figure 1 The grid distribution in the meridian plane and the equatorial plane, where the black quadrilaterals denote the grid cells cut through the *x*-*z* plane and the *x*-*y* plane. Color contours of current density J_y are plotted to delineate magnetospheric boundaries, such as the magnetopause and the bow shock. A white sphere of radius 3.0 R_E plotted near the planet represents the inner boundary of the model. Note that high resolution grids are placed in the bow shock, the magnetopause, and the magnetotail.

Initially, the computational domain in every reference component is divided into 10 × 4 × 4 blocks with each block consisting of 8 × 8 × 8 cells. These correspond to $N_\theta = N_\varphi = 33$, where N_θ and N_φ are the mesh numbers of the latitude and longitude, respectively. Thus, $\Delta\theta = (\theta_{\max} - \theta_{\min})/(N_\theta - 1) = \pi/64$, $\Delta\varphi = (\varphi_{\max} - \varphi_{\min})/(N_\varphi - 1) = \pi/64$. The gird points on each component in physical space is defined as $\theta_j = \theta_{\min} + j\Delta\theta$, $j = 0,1,\cdots, N_\theta - 1$, and $\varphi_k = \varphi_{\min} + k\Delta\varphi$, $k = 0, 1, \cdots, N_\varphi - 1$, where $\theta_{\min} = \pi/4$, $\theta_{\max} = 3\pi/4$, $\varphi_{\min} = 3\pi/4$, and $\varphi_{\max} = 5\pi/4$. The inner boundary is set at $r = 3.0$ R_E and the outer boundary is set at $r = 156.0$ R_E such that each component of the physical grids is equivalent to $2.797 < \xi < 12.86$, $\pi/4 - \delta \leqslant \eta \leqslant 3\pi/4 + \delta$, and $3\pi/4 - \delta \leqslant \zeta \leqslant 5\pi/4 + \delta$ in the computational domain or the reference space.

There exists a nonsingular curvilinear coordinate transform (Feng et al., 2012a) between the reference coordinates (ξ, η, ζ) and the physical coordinates (x, y, z) such that the model equation (1) can be expressed in the reference coordinates (ξ, η, ζ) as

$$\frac{\partial \hat{\mathbf{U}}}{\partial t} + \left[\nabla \cdot \left(\hat{\tilde{\mathbf{F}}} - \hat{\tilde{\mathbf{F}}}_v\right)\right]^T = \hat{\mathbf{S}}, \tag{9}$$

where the corresponding transformation of coordinates between any two components or transformation of solution variables between $(\hat{\mathbf{U}}, \hat{\tilde{\mathbf{F}}}, \hat{\tilde{\mathbf{F}}}_v)$ in the reference space and $(\mathbf{U}, \tilde{\mathbf{F}}, \tilde{\mathbf{F}}_v)$ in the physical space on an arbitrary component have been provided by Feng et al. (2010, 2013, 2014). Note that eq. (9) in the reference coordinate space (ξ, η, ζ) can be solved directly by the CESE solver (Feng et al., 2007, 2010) with rectangular box cells in a logically Cartesian space.

With these in mind, we can easily take turns between the physical-solution variables and the reference-solution variables. That is, if the initial inputs of the physical solution variables are given, we first use $\tilde{\mathbf{F}}$, $\tilde{\mathbf{F}}_v$ to calculate the fluxes $\hat{\tilde{\mathbf{F}}}$, $\hat{\tilde{\mathbf{F}}}_v$ and apply the CESE solver to eq. (9) to obtain the reference-solution variables $\hat{\mathbf{U}}$ and their first-order derivatives $(\hat{\mathbf{U}}_\xi, \hat{\mathbf{U}}_\eta, \hat{\mathbf{U}}_\zeta)$ at the new time step. Finally, we can recover the physical solution variables $(\mathbf{U}, \mathbf{U}_x, \mathbf{U}_y, \mathbf{U}_z)$.

2 Simulation results

We have solved the MHD Equations by using the AMR-CESE-MHD method on a six-component grid system. The model is driven by steady solar wind with due northward IMF. When $\frac{\|\mathbf{U}^{n+1} - \mathbf{U}^n\|}{\|\mathbf{U}^n\|} < 10^{-6}$ is satisfied during the code running, the numerical results can be believed to arrive at a quasi-steady state and we get the corresponding quasi-steady state of the magnetospheric configurations.

The computational domain extends from 3.0 to 156.0 R_E. The magnetic field is so strong near the Earth's surface that the Alfvén velocity becomes very high. In order to keep the computation time step from becoming too small, we set the inner boundary at 3.0 R_E. Figure 1 shows the grid distribution in the meridian plane and the equatorial plane, where the black quadrilaterals denote the grid cells cut through the *x*-*z* plane and the *x*-*y* plane. Color contours of current density J_y are plotted to delineate magnetospheric boundaries, such as the magnetopause and the bow shock. The grid size varies from 0.15 R_E near the inner boundary to be 3.8 R_E downstream far from the Earth.

Figure 2 shows the color contours of density, velocity, thermal pressure, and logarithmic magnetic strength for due northward IMF case. The locations and shapes of the bow shock and the magnetopause can be clearly seen from this figure, respectively.

When the solar wind meets the Earth's magnetosphere, bow shock forms before the planet's magnetopause. At the same time, the solar wind is heated and decelerated while coming across the bow shock, and then it is deflected to flow away around the magnetopause. It is worthy to note that two funnel-shaped regions with high speed flow located at the nightside of cusp region, where the magnetic field is very weak. They are related to the cusp reconnection during the northward IMF conditions. The distribution of V_x in the *x*-*z* plane shows weak sunward flows ($0 < V_x < 50$ km s^{-1}) in the magnetosphere driven by reconnection or the global

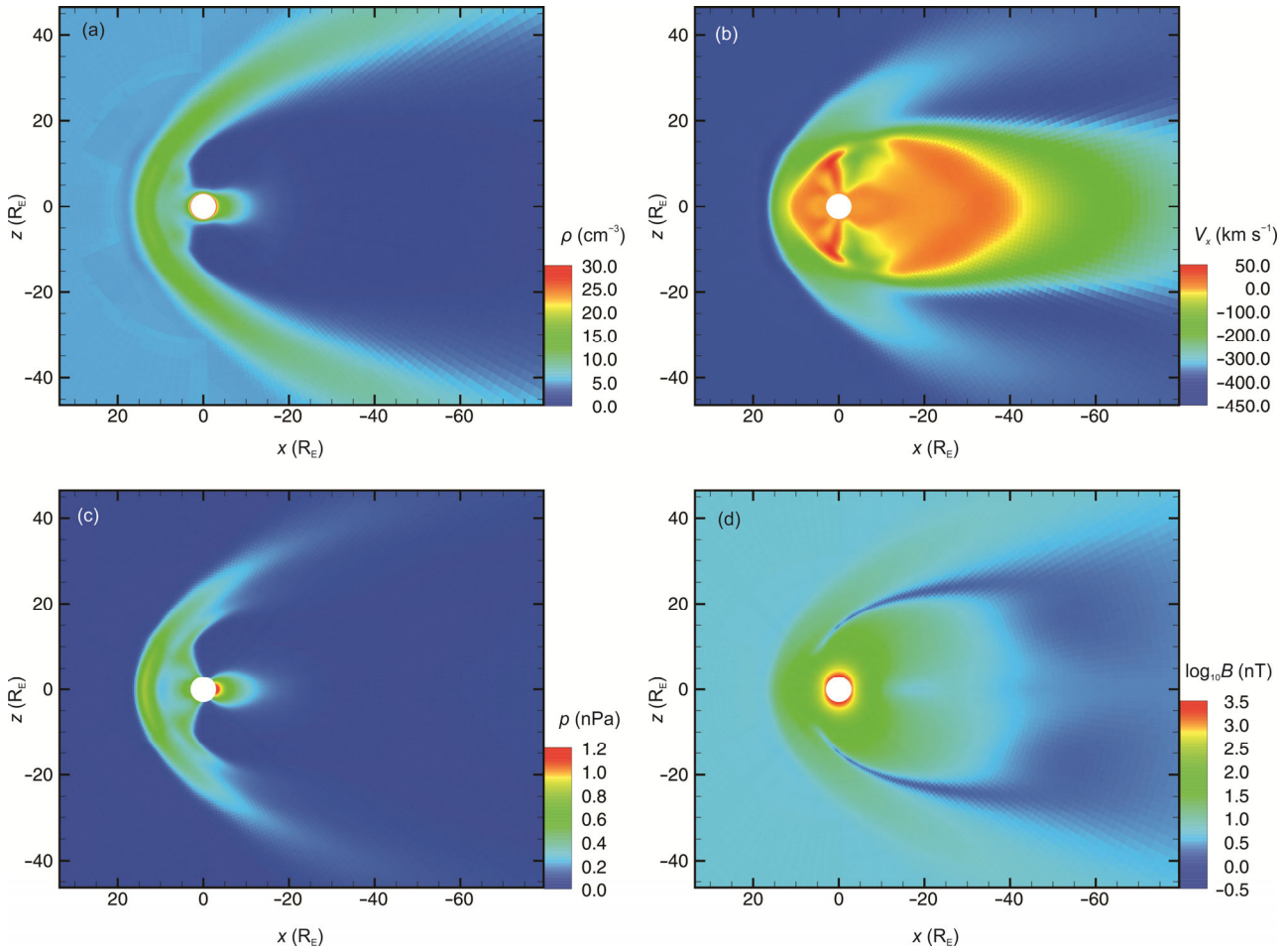

Figure 2 Color contours of density (a), velocity (b), pressure (c), and the logarithmic magnetic strength (d) for due northward IMF case.

convection electric field. We extract R_{BS} (the subsolar bow shock standoff distance) by locating the bow shock at the midpoint of the MHD jump in velocity along the *x*-axis and the R_{BS} are 15.5 R_E for due northward IMF.

Figure 3 clearly shows the color contours of the current density and thermal pressure under due northward IMF in the cross section at $x = -15.0$ R_E in the tail. A θ-shaped configuration turns up in the cross sections. The current density in the bow shock with ~10^{-4} μA m^{-2} (outer turquoise-color circle) is much lower than the magnetopause current density with ~4×10^{-4} μA m^{-2}. Plots of the current density clearly show that the magnetopause currents and the cross-tail currents form a closed system. The cross-tail current sheet is horizontal because our present tests have been run with no dipole tilt. Moreover, we find that the θ-shaped configuration under due northward IMF is flat.

We present the distribution of the *y*-direction current density J_y on the noon-midnight meridian plane in Figure 4 in which the red lines with arrowheads are the magnetic field lines. From Figure 4, we can see that the magnetosphere is closed under due northward IMF. The tail of the closed magnetosphere extends to nearly 50.0 R_E (denoted by a gray dot). Our results show that the reconnection between the IMF and the magnetospheric field takes place on the nightside of the two cusp regions for northward IMF. This was first proposed by Dungey (1961). And the cusp reconnection has been shown in these simulation models summarized by the introduction of this paper. We find that the location of the dayside magnetopause defined by the last closed magnetic field line is located at 11.2 R_E (denoted by a blue dot) in the subsolar region, 14.8 R_E (denoted by a white dot) at the noon-midnight terminators. Our results are well consistent with the empirical magnetopause location according to Shue et al. (1998).

At the bow shock, currents are generated. The solar wind flow is decelerated by the Lorentz force owing to these currents. The dayside magnetopause current is present near the region of the first closed magnetic field line (dayside magnetopause). The y-direction current density peaks away from the equator and extends to higher latitude along the field lines (Meng et al., 2012). However, the nightside magnetopause current and the topology of the magnetopause become completely different on the nightside (Song et al., 1999), so we cannot directly determine the nightside

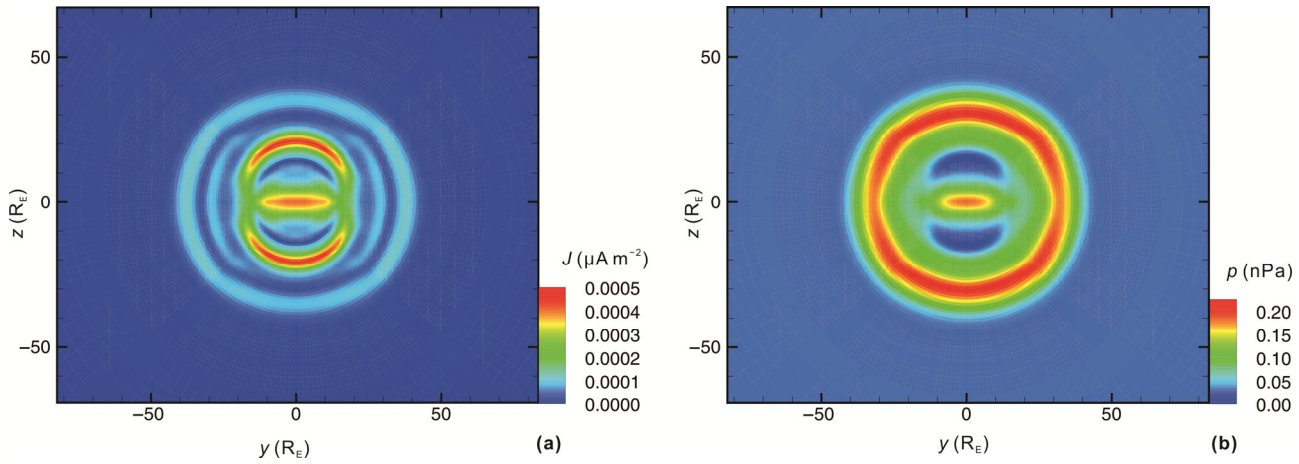

Figure 3 Plots of the current density J (a) and thermal pressure (b) color contours for due northward IMF in the cross sections at $x = -15.0$ R_E in the tail.

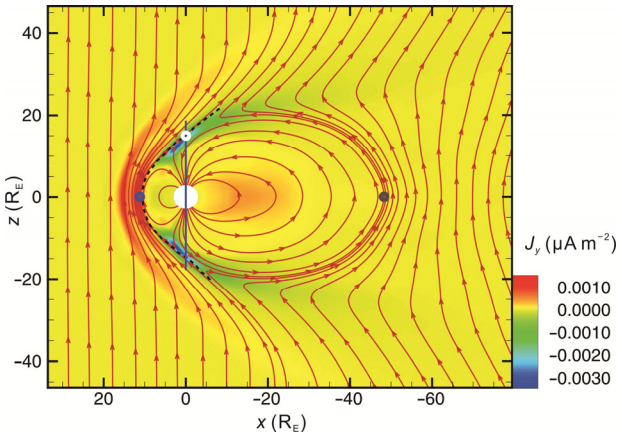

Figure 4 Color contours of the current J_y plotted under the traces of magnetic field lines for due northward IMF.

magnetopause by locations of the nightside magnetopause current.

Figure 5 shows the distributions of ionospheric field-aligned currents and electric potential in the ionospheric northern hemisphere for northward IMF in an MLT-magnetic latitude coordinate system. Figure 5(a) shows that three pairs of field-aligned currents turn up in the ionosphere under due northward IMF. The closest to the magnetic pole is the pair of the Northward B_z (NBZ) currents. Following the NBZs currents, region-1 and region-2 currents are distributed equatorward in the ionosphere (Song et al. (1999)). Yet region-2 currents are so weak that we can hardly make out them. The four-cell structure of electric potential is shown in Figure 5(b). It is interesting that the two dayside cells look like bananas while the two nightside cells look like mangos.

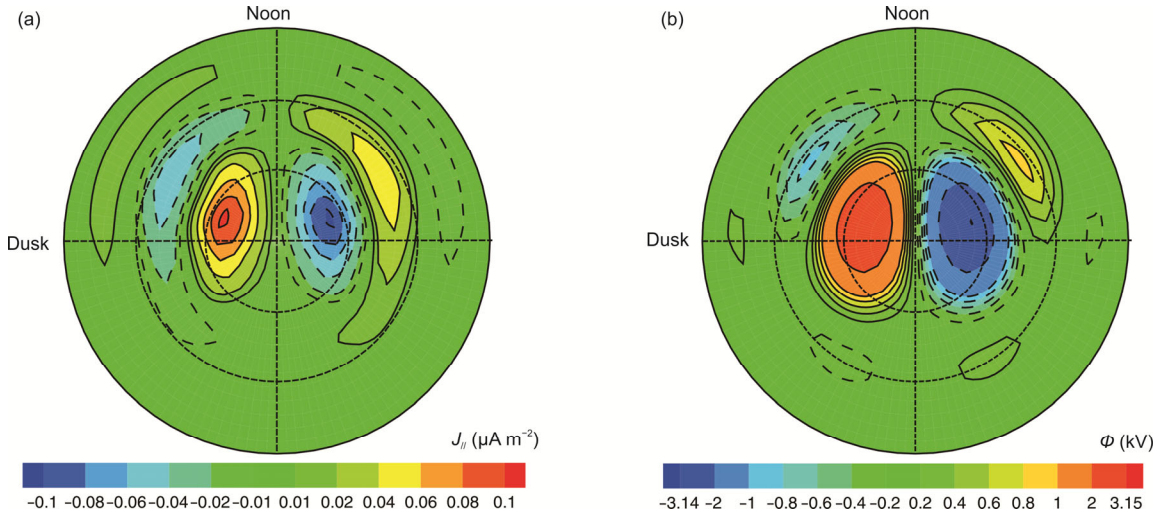

Figure 5 The distributions of ionospheric field-aligned currents $J_{//}$ (a) and electric potential Φ(b) in the Northern Hemisphere for due northward IMF, in an MLT-magnetic latitude coordinate system. The outermost solid circle shows the 58.8° latitude, and the dashed concentric circles correspond to 70° latitude and 80° latitude. The blue/green colors in (a) represent the outflow currents and yellow/red colors represent the inflow currents.

Typically structures such as the bow shock, the magnetosphere and the current sheet are all well reproduced by our simulations. Our results are comparable to those published by other researchers (Song et al., 1999; Guzdar et al., 2001; Kabin et al., 2004; Lavraud and Borovsky, 2008; Ridley et al., 2010; Zhang et al., 2011; Meng et al., 2012).

3 Discussions and conclusions

We have used the AMR-CESE-MHD method on a six-component grid system to simulate the Earth's magnetosphere under steady solar wind with due northward IMF for model validation. The code was running on a highly parallel computer with 96 processes.

We have used two levels grid refinement by using the AMR technique and the discontinuity in the computational domain such as the bow shock, the magnetopause are all captured very well. Our test results are highly consistent with the simulation results provided by the Community Coordinated Modeling Center (CCMC) at Goddard Space Flight Center through their public Runs on Request system (http://ccmc.gsfc.nasa.gov).

As a milestone physics-based model of space weather study, the CESE-MHD model developed by Feng and his colleagues (Hu et al., 2008; Yang et al., 2011; Jiang and Feng, 2012, 2013; Zhou et al., 2012, 2013, 2014; Feng et al., 2014) has the following merits. (1) The combination of the projected normal characteristic method and the mass flux limit enables the model to reproduce reasonable distributions of the plasma density, temperature and velocity on the solar surface and incorporation of the time-dependent magnetograms into the model is preliminarily established (Feng et al., 2012c; Yang et al., 2012), with emphasis focused on how to preprocess the observational data, how to solve projected normal characteristics equations, and how to update the bottom boundary by using the time-dependent magnetic field from either observations or the surface flux transport model. (2) The CESE MHD model provides a unified treatment of flow evolution in space and time and keeps the local and global space-time flux conservation in a coherent and efficient manner. The fluxes at the interface of any pair of conservation elements (CEs) can be efficiently evaluated by means of non-staggered space-time grids without using Riemann solvers or other flux models, which significantly reduces the CPU time. (3) The treatment of time iteration by integrating two half timesteps into one full timestep (Jiang et al., 2010; Feng et al., 2012a) leads to low-storage and makes the scheme suitable for building blocks for adaptive mesh refinement calculations. (4) The introduction of six-component grid (Feng et al., 2010, 2014) for the computational domain enables us to fit the spherical surface boundary with an easy implementation of the inner boundary conditions, and meanwhile to avoid both coordinate singularities and polar grid convergence. Particularly, it will be easy to recognize the observation at the lower boundary. This property of course applies to the spherical computational domain of magnetospheric study. (5) It should be noted that the same CESE solver can apply to any coordinate system (such as Cartesian, spherical, cylindrical coordinates and any other curvilinear coordinates) with only the difference of the coordinate transformation, and consequently the solver is highly independent of the grid system.

All these above advantages of CESE-MHD model can be explored in the future to improve the present model in this paper for magnetospheric study in the following aspects, such as numerical accuracy, stability, grid resolution and time-dependent solar wind input. Especially, the time-varying results (at the Earth) obtained by the CESE-MHD model for a coronal mass ejection from the Sun to the Earth can be used as input to our MHD model here for studying the influence of adverse space weather on the Earth's magnetosphere and ionosphere in more realistic way.

On the other hand, the closer loop of the Pederson current has not been well-known. The CESE-MHD model is helpful to building the ionospheric current system during the northward IMF conditions (Du et al., 2008, 2011a, b; Xu et al., 2008).

The work was supported by the National Basic Research Program of China (Grant Nos. 2012CB825601, 2014CB845903, 2012CB825604), the National Natural Science Foundation of China (Grant Nos. 41031066, 41231068, 41274192, 41074121, 41204127, 41174122), the Knowledge Innovation Program of the Chinese Academy of Sciences (Grant No. KZZD-EW-01-4), and the Specialized Research Fund for State Key Laboratories.

Du A M, Tsurutani B T, Sun W. 2008. Anomalous geomagnetic storm of 21-22 January 2005: A storm main phase during northward IMFs. J Geophys Res, 113: A10214

Du A M, Sun W, Tsurutani B T, et al. 2011a. Observations of dawn-dusk aligned polar cap aurora during the substorms of January 21, 2005. Planet Space Sci, 59: 1551–1558

Du A M, Tsurutani B T, Sun W. 2011b. Solar wind energy input during prolonged, intense Northward interplanetary magnetic fields: A new coupling function. J Geophys Res, 116: A12215

Dungey J W. 1961. Interplanetary magnetic field and the auroral zones. Phys Rev Lett, 6: 47–48

Feng X S, Zhou Y F, Wu S T. 2007. A novel numerical implementation for solar wind modeling by the modified conservation element/solution element method. Astrophys J, 655: 1110–1126

Feng X S, Yang L P, Xiang C Q, et al. 2010. Three-dimensional solar wind modeling from the Sun to Earth by a SIP-CESE MHD model with a six-component grid. Astrophys J, 723: 300–319

Feng X, Zhang S, Xiang C, et al. 2011. A hybrid solar wind model of the CESE+HLL method with a Yin-Yang overset grid and an AMR grid. Astrophys J, 734: 50

Feng X, Yang L, Xiang C, et al. 2012a. Validation of the 3D AMR SIP-CESE solar wind model for four carrington rotations. Solar Phys, 279: 207–229

Feng X S, Jiang C W, Xiang C Q, et al. 2012b. A data-driven model for the global coronal evolution. Astrophys J, 758: 62

Feng X S, Yang L P, Xiang C Q, et al. 2012c. Numerical study of the global corona for CR 2055 driven by daily updated synoptic magnetic field. In: Pogorelov N V, Font J A, Audit E, et al., eds. Numerical modeling of space plasma slows (ASTRONUM 2011). Astron Soc Pacific Conf Ser, 459: 202–208

Feng X, Zhong D, Xiang C, et al. 2013. GPU-accelerated computing of three-dimensional solar wind background. Sci China Earth Sci, 56: 1864–1880

Feng X, Xiang C, Zhong D, et al. 2014. SIP-CESE MHD model of solar wind with adaptive mesh refinement of hexahedral meshes. Comput Phys Commun, 185: 1965–1980

Gombosi T I, DeZeeuw D L, Groth C P T, et al. 1998. The length of the magnetotail for northward IMF: Results of 3D MHD simulations. Phys Space Plasmas, 15: 121–128

Guzdar P N, Shao X, Goodrich C C, et al. 2001. Three-dimensional MHD simulations of the steady state magnetosphere with northward interplanetary magnetic field. J Geophys Res, 106: 275–287

Hu Y Q, Guo X C, Li G Q, et al. 2005. Oscillation of quasi-steady Earth's magnetosphere. Chin Phys Lett, 22: 2723

Hu Y Q, Feng X S, Wu S T, et al. 2008. Three-dimensional MHD modeling of the global corona throughout solar cycle 23. J Geophys Res, 113: A03106

Janhunen P, Palmroth M, Laitinen T, et al. 2012. The GUMICS-4 global MHD magnetosphere-ionosphere coupling simulation. J Atmos Solar-Terr Phys, 80: 48–59

Jiang C W, Feng X S. 2012. A new implementation of the magnetohydrodynamics-relaxation method for nonlinear force-free field extrapolation in the solar corona. Astrophys J, 749: 135

Jiang C W, Feng X S. 2013. Extrapolation of the solar coronal magnetic field from SDO/HMI magnetogram by a CESE-MHD-NLFFF code. Astrophys J, 769: 144

Jiang C W, Feng X S, Zhang J, et al. 2010. AMR simulations of magnetohydrodynamic problems by the CESE Method in curvilinear coordinates. Solar Phys, 267: 463

Jing H, Lu J Y, Kabin K, et al. 2014. MHD simulation of energy transfer across magnetopause during sudden changes of the IMF orientation. Planet Space Sci, 97: 50–59

Kabin K, Rankin R, Rostoker G, et al. 2004. Open-closed field line boundary position: A parametric study using an MHD model. J Geophys Res, 109: A05222

Lavraud B, Borovsky J E. 2008. Altered solar wind-magnetosphere interaction at low Mach numbers: Coronal mass ejections. J Geophys Res, 113: A00B08

Liu Z Q, Lu J Y, Kabin K, et al. 2012. Dipole tilt control of the magnetopause for southward IMF from global magnetohydrodynamic simulations. J Geophys Res, 117: A07207

Lu J Y, Liu Z Q, Kabin K, et al. 2011. Three dimensional shape of the magnetopause: Global MHD results. J Geophys Res, 116: A09237

Lu J Y, Jing H, Liu Z Q, et al. 2013. Energy transfer across the magnetopause for northward and southward interplanetary magnetic fields. J Geophys Res, 118: 2021–2033

Lyon J G, Fedder J A, Mobarry C. 2004. The Lyon-Fedder-Mobarry (LFM) global MHD magnetospheric simulation code. J Atmos Solar-Terr Phys, 66: 1333–1350

MacNeice P, Olson K M, Mobarry C, et al. 2000. PARAMESH: A parallel adaptive mesh refinement community toolkit. Comput Phys Commun, 126: 330–354

Meng X, Tóth G, Liemohn M W, et al. 2012. Pressure anisotropy in global magnetospheric simulations: A magnetohydrodynamics model. J Geophys Res, 117: A08216

Merkin V G, Lyon J G. 2010. Effects of the low-latitude ionospheric boundary condition on the global magnetosphere. J Geophys Res, 115: A10202

Ogino T. 1986. A three-dimensional MHD simulation of the interaction of the solar wind with the Earth's magnetosphere: The generation of field-aligned currents. J Geophys Res, 91: 6791–6806

Ogino T, Walker R J, Ashour-Abdalla M. 1994. A global magnetohydrodynamic simulation of the response of the magnetosphere to a northward turning of the interplanetary magnetic field. J Geophys Res, 99: 11027–11042

Powell K G, Roe P L, Linde T J, et al. 1999. A solution-adaptive upwind scheme for ideal magnetohydrodynamics. J Comput Phys, 154: 284–309

Rae I J, Kabin K, Lu J Y, et al. 2010. Comparison of the open-closed separatrix in a global magnetospheric simulation with observations: The role of the ring current. J Geophys Res, 115: A08216

Raeder J. 2003. Global magnetohydrodynamics—A tutorial. In: Buvhnrt J, Dum C T, Scholer M, eds. Space Plasma Simulation. Lectures Notes Phys, 615: 212–246

Raeder J, Berchem J, Ashour-Abdalla M. 1998. The geospace environment modeling grand challenge: Results from a global geospace circulation model. J Geophys Res, 103: 14787– 14797

Ridley A J, Gombosi T I, Sokolov I V, et al. 2010. Numerical considerations in simulating the global magnetosphere. Ann Geophys, 28: 1589–1614

Shue J H, Song P, Russell C T, et al. 1998. Magnetopause location under extreme solar wind conditions. J Geophys Res, 103: 17691–17700

Song P, DeZeeuw D L, Gombosi T I, et al. 1999. A numerical study of solar wind-magnetosphere interaction for northward interplanetary magnetic field. J Geophys Res, 104: 28361–28378

Tanaka T. 1994. Finite volume TVD scheme on an unstructured grid system for three-dimensional MHD simulation of inhomogeneous systems including strong background potential fields. J Comput Phys, 111: 381–389

Tóth G, Sokolov I V, Gombosi T I, et al. 2005. Space weather modeling framework: A new tool for the space science community. J Geophys Res, 110: A12226

Wang C, Li H, Guo X, et al. 2012. Numerical study on the response of the Earth's magnetosphere-ionosphere system to a super solar storm. Sci China Earth Sci, 55: 1037–1042

Xu W Y, Chen G X, Du A M, et al. 2008. Key points model for polar region currents. J Geophys Res, 113: A03S11

Yang L P, Feng X S, Xiang C Q, et al. 2011. Simulation of the unusual solar minimum with 3D SIP-CESE MHD model by comparison with multi-satellite observations. Solar Phys, 271: 91–110

Yang L P, Feng X S, Xiang C Q, et al. 2012. Time-dependent MHD modeling of the global solar corona for year 2007: Driven by daily-updated magnetic field synoptic data. J Geophys Res, 117: A08110

Zhang B, Lotko W, Wiltberger M J, et al. 2011. A statistical study of magnetosphere–ionosphere coupling in the Lyon-Fedder-Mobarry global MHD model. J Atmos Solar-Terr Phys, 73: 686–702

Zhou Y F, Feng X S, Wu S T, et al. 2012. Using a 3-D spherical plasmoid to interpret the Sun-to-Earth propagation of the 4 November 1997 coronal mass ejection event. J Geophys Res, 117: A01102

Zhou Y F, Feng X S. 2013. MHD numerical study of the latitudinal deflection of coronal mass ejection. J Geophys Res, 118: 6007–6018

Zhou Y F, Feng X S, Zhao X H. 2014, Using a 3-D MHD simulation to interpret propagation and evolution of a coronal mass ejection observed by multiple spacecraft: The 3 April 2010 event. J Geophys Res, 119: 9321–9333